Mass independent fractionation of even and odd mercury isotopes during atmospheric mercury redox reactions

Xuewu Fu[†,‡], Martin Jiskra[†, §], Xu Yang[†], Nicolas Marusczak[†], Maxime Enrico[†], Jerome Chemleff[†], Lars-Eric Heimbürger-Boavida[†,%] François Gheusi[‖], Jeroen E. Sonke[†,*]

[†] Géosciences Environnement Toulouse, CNRS/IRD/CNRS/Université de Toulouse, France

[‡] State Key Laboratory of Environmental Geochemistry, Institute of Geochemistry, Chinese Academy of Sciences, Guiyang, 550081, China.

[§] Environmental Geosciences, University of Basel, Switzerland

[‖] Laboratoire d'Aérologie, CNRS/IRD/Université de Toulouse, France

[%] Mediterranean Institute of Oceanography, Aix Marseille Université, CNRS/IRD, Université de Toulon, IRD, Marseille, France

* Corresponding Author: jeroen.sonke@get.omp.eu

Keywords: MDF, MIF, MIE, Hg stable isotopes, free troposphere, magnetic isotope effect, radical photochemistry, reduction

Synopsis: Novel Hg isotope observations of gaseous oxidized Hg, cloudwater and rainfall document Hg MIF during atmospheric redox cycling

Abstract. Mass independent fractionation (MIF) of even mass number mercury (Hg) stable isotopes is observed in rainfall and gaseous elemental Hg^0 globally, and is used to quantify atmospheric Hg deposition pathways. The chemical reaction and underlying even-Hg MIF mechanism are unknown however, and speculated to be caused by Hg photo-oxidation on aerosols at the tropopause. Here we investigate the Hg isotope composition of free tropospheric Hg^0 and oxidized Hg^{II} forms at the high altitude Pic du Midi Observatory. We find that gaseous oxidized Hg has positive Δ^{199}Hg, Δ^{201}Hg, Δ^{200}Hg, and negative Δ^{204}Hg signatures, similar to rainfall Hg, and we document rainfall Hg Δ^{196}Hg to be near-zero. Cloud water and rainfall Hg show enhanced odd-Hg MIF of 0.3‰ compared to gaseous oxidized Hg^{II}, potentially indicating the occurrence of in-cloud aqueous Hg^{II} photoreduction. Diurnal MIF observations of free tropospheric Hg^0 show how net Hg^0 oxidation in high altitude air masses leads to opposite even- and odd-MIF in Hg^0 and oxidized Hg^{II}. We speculate that even-Hg MIF takes place by a molecular magnetic isotope effect during Hg^{II} photoreduction on aerosols that involves magnetic halogen nuclei. A Δ^{200}Hg mass balance suggests that global Hg deposition pathways in models are likely biased towards Hg^{II} deposition. We propose that Hg cycling models could accommodate the Hg-isotope constraints on emission and deposition fluxes.

TOC abstract:

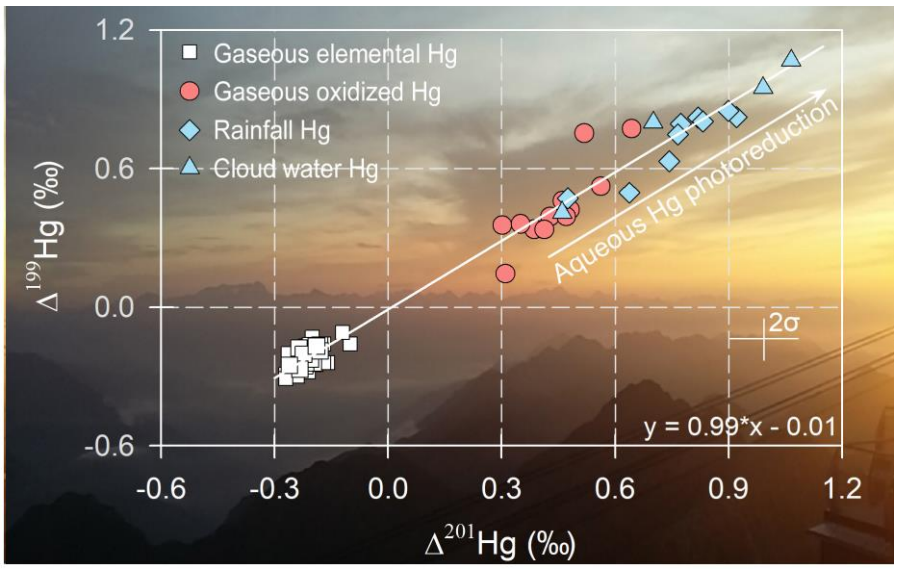

1. Introduction

Modern anthropogenic Hg emissions to air (2400 Mg a^{-1}) outweigh natural Hg emissions (340 Mg a^{-1}) by an order of magnitude.[1, 2] Hg emissions are mostly in the form of gaseous elemental Hg (GEM), which has a long (3 months) atmospheric life-time against oxidation to divalent reactive Hg (RM) forms that include gaseous oxidized Hg (GOM) and particulate bound Hg (PBM).[3] RM is rapidly deposited to continental and marine ecosystems where microbial and abiotic activity transforms a fraction of inorganic Hg into the bioaccumulating and toxic methylmercury form.[4, 5] Predicting the impact of anthropogenic Hg emission scenarios on global Hg deposition requires detailed understanding of atmospheric Hg emissions, transformation mechanisms, and deposition pathways. Two decades of atmospheric Hg research using mountain-top and in-flight observations, experimental and theoretical reaction kinetics, and coupled 3D atmosphere-ocean chemistry and transport models, have given broad understanding of atmospheric Hg dynamics.[6-10] Experimental, theoretical and modeling studies suggest Hg oxidation initiated by bromine (Br) radicals to be faster than by ozone or OH,[3, 11] yet major uncertainties in RM concentrations, oxidation and reduction mechanisms and rates remain.[12-14] Hg primary emission budgets from natural volcanic, and anthropogenic sources are known to within 30%,[1, 2] yet re-emission fluxes from terrestrial and marine environments remain uncertain.[15] Similarly, atmospheric Hg deposition pathways, which include RM wet and dry deposition, and terrestrial and marine GEM uptake are not well constrained.[16]

Hg stable isotope analysis of atmospheric Hg compounds may provide new information on Hg emission sources and complex atmospheric redox cycling. During the last decade, significant advances have been made in the measurement of Hg isotope compositions of biogeochemical reservoirs.[17] Laboratory and field evidence suggests that processes controlling Hg emission such as reduction/oxidation, adsorption/desorption, or volatilization can induce significant mass dependent Hg isotope fractionation (MDF, δ^{202}Hg signature).[18-20] Large mass independent Hg isotope fractionation (MIF) of odd Hg isotopes by the magnetic isotope effect (MIE) has been observed in aqueous photochemical Hg reduction experiments (Δ^{199}Hg, Δ^{201}Hg signatures).[21, 22] Small MIF variability can also occur due to the nuclear volume effect (NVE).[23] Large odd-MIF signatures imparted on inorganic Hg and methyl-Hg by photochemistry can be traced into all Earth surface environments, i.e sediments, biota, atmosphere, soils etc, and helps quantify sources, and Hg transformations. More unusual, even isotope MIF (Δ^{200}Hg, Δ^{204}Hg signatures) has been observed in oxidized Hg forms in rainfall and snowfall globally,[24-26] and has been speculated to originate in GEM photo-oxidation at and above the tropopause.[24] Because even-MIF does not seem to occur measurably during Hg transformation at the Earth's surface, it has

become a useful tracer for atmospheric deposition pathways, or sources of Hg to land and oceans.[27, 28] Yet, the exact even-MIF mechanism and even-MIF inducing Hg transformation(s) remain essentially unknown.

In this study we investigate Hg isotope composition of GEM, RM, and cloud water at the high altitude Pic du Midi Observatory (PDM, 2877m, France). The PDM regularly receives free tropospheric air masses that are enriched in RM and depleted in GEM.[29] High frequency, 12h and 24h GEM isotope observations of a free tropospheric air mass rich in GOM and depleted in GEM are investigated to derive MDF and MIF factors for net oxidation. A photoreduction experiment on rainfall is made to investigate atmospheric aqueous MDF and MIF. We investigate the even-MIF on the low abundance ^{196}Hg isotope to help understand potential even-Hg MIF mechanisms, and we review previous even-Hg MIF to speculate on a potential heterogeneous photoreduction mechanism. Finally, we use a Hg isotope emission and deposition mass balance to illustrate bias of state of the art Hg cycling models towards RM deposition.

2. Materials and methods

2.1 Atmospheric sampling and processing

Short-term (12/24h) variations in atmospheric GEM isotopic composition were investigated during a 10-day sampling campaign, from 19 to 28 in Dec 2012, at the Pic du Midi Observatory, France (PDM, 0.14º E, 42.94º N, 2877 m a.s.l) using chlorine-impregnated activated carbon (CLC) traps (Text S1 and S2).[30] Atmospheric Hg speciation at the PDM, including GEM, GOM and PBM, was continuously measured during the campaign with a Tekran 2537/1130/1135 system (Tekran Inc., Canada, Text S3).[29, 31] Seven day backward trajectories ending at PDM at a height of 3000 m above sea level were calculated every 2 hours, during the campaign, with simulated gridded meteorological data from the Weather Research and Forecasting (WRF) model Version 3.4 (Text S4). CLC traps were thermally decomposed (25 ºC to 1000 ºC over 8h) in a Hg-free oxygen flow (25 ml min^{-1}) in a tube furnace. Combustion products were further decomposed in a 2nd pyrolizer tube furnace at 1000 °C, and purged into a 10 ml 40 vol% HNO_3:HCl (2:1 ratio) oxidizing solution.[32] CLC sampling efficiencies were better than 95%, mean recovery efficiencies were 87%, and full procedural blanks <2% of Hg concentrations in trapping solutions.[30]

Twelve samples of the atmospheric RM (RM=GOM+PBM) were obtained using Millipore polyethersulfone cation exchange membranes (CEMs, Millipore, 0.45 µm pore size, 47 mm and 90 mm diameter) at the PDM from June to October 2014, with sampled air volumes between 25 and 77 m^3.[31] Cloud water samples were collected from July to November 2014 with a CASCC-2 sampler at the PDM.[33] Rainfall was sampled from

July to August 2014 150 km downwind from the PDM at 800m altitude in the Pyrenees foothills using acid-washed (0.1N HCl, 3x MQ water rinsed) polypropylene buckets and reported elsewhere.[27] Snowfall and rainfall was collected at the PDM and the Geosciences Environnement Toulouse (GET, Toulouse, France, 43.54º N, 1.48º E) laboratory between 2016 and 2017 using the same methods. All sampling was event-based in order to avoid evaporation, and samples were acidified to 0.04 N HCl immediately after sampling, except for a single incubation rainfall sample. Cloud water, rainfall and snowfall samples were pre-concentrated by reducing and purging Hg with $SnCl_2$ and a clean argon flow and subsequent trapping in an oxidizing solution.[34] Recoveries of procedural standards, RM, rainfall and cloud water samples was >95%. RM on CEMs was leached in 20 vol% $2HNO_3/1HCl0$ with blanks <4% of sampled RM. In this study we assume that all Hg in RM, cloud water, rainfall and snowfall was present as Hg(II).

Hg isotope fractionation during aqueous photochemical reduction of rainwater was studied using a solar simulator (see Yang *et al* for details).[35] A low Hg level (2.6 ng L^{-1}) rainfall sample 'GET rain 4' obtained at GET was spiked with 103 ng L^{-1} NIST 3133 and equilibrated for 48h in the dark. A 450 mL aliquot was then transferred into an acid-cleaned quartz reactor, and illuminated for 24h with the solar spectrum from a Xe lamp. The measured UVB, UVA, and VIS light intensities were 25, 186, 242 W m^{-2} respectively. The sample was continuously purged with Hg-free Ar gas to remove reaction product Hg^0 and avoid photo-oxidation. After 24h, the 78 ng L^{-1} dissolved Hg(II) remaining in the 450mL reactor volume was transferred to a pre-cleaned 1L Pyrex bottle, and pre-concentrated for Hg isotope analysis.

2.2 Hg isotope analysis

Hg isotope ratios were measured using cold vapor multi-collector inductively coupled plasma mass spectrometry (CV-MC-ICPMS, Thermo-Finnigan Neptune Plus) at the Midi-Pyrenees Observatory, Toulouse, France following the methods described in previous studies.[34, 36] Despite different sampling years, all samples were processed and analyzed in the weeks following sampling. Instrumental mass bias of MC-ICPMS was corrected by standard-sample-standard bracketing using NIST3133 Hg at matching concentrations. Hg isotopic composition is reported in delta notation (δ) in units of per mil (‰) referenced to the bracketed NIST 3133 Hg standard:[37]

$$\delta^{xxx}Hg = [(^{xxx}Hg/^{198}Hg)_{sample}/(^{xxx}Hg/^{198}Hg)_{NIST3133} -1] \qquad (1)$$

where xxx represent Hg isotope masses 196, 199, 200, 201, 202, 204. MIF values are expressed by "capital delta (Δ)" notation (‰), which is the difference between the measured values of $\delta^{196}Hg$, $\delta^{199}Hg$, $\delta^{200}Hg$, $\delta^{201}Hg$

and those predicted from δ^{202}Hg using the kinetic MDF law: [37]

$$\Delta^{xxx}\text{Hg (‰)} = \delta^{xxx}\text{Hg} - (\beta^{xxx} \times \delta^{202}\text{Hg}) \qquad (2)$$

where β^{xxx} is -0.5074, 0.2520, 0.5024, 0.7520, 1.493 for the 196, 199, 200, 201, and 204 Hg isotopes respectively. The analytical uncertainty of isotopic analysis was assessed by repeated analysis of the UM-Almaden and ETH-Fluka standards over different analysis sessions and at Hg concentrations corresponding to the samples. The overall mean values of δ^{202}Hg, Δ^{199}Hg, Δ^{200}Hg, Δ^{201}Hg, and Δ^{204}Hg for all the UM-Almaden standards in the 0.5 to 1.5 ng g^{-1} range were -0.56 ± 0.07 ‰, -0.04 ± 0.08 ‰, -0.01 ± 0.09 ‰ and -0.05 ± 0.09 ‰, and 0.04 ± 0.19 ‰ (2SD, n = 11) respectively, which agree well with previously reported values.[38] The procedural standard for rainfall pre-concentration, i.e. rainfall sample 'GET rain 4' spiked with 103 ng g^{-1} NIST 3133 showed good recovery, and δ^{xxx}Hg values not significantly different from zero (Table S3). In the present study, the analytical uncertainty of CV-MC-ICPMS isotope analysis of RM, GEM, rainfall, and snowfall is the 2SD uncertainty of the UM-Almaden standard, unless the 2SD uncertainty on repeated analysis of the same sample over different analytical sessions was larger.

To attempt rainfall Δ^{196}Hg analysis, we screened rainfall samples obtained at GET in 2016 for both high Hg concentration levels and high volume single events. Rainfall sample 'GET rain 6' was the only sample retained as it consisted of a single thunderstorm event of 20.5 L, collected in the 8 large buckets, and had a Hg concentration of 6.0 ng L^{-1}. The entire 20.5L volume was pre-concentrated 1200x in a single large 25L Pyrex glass bottle to a final concentration of 8.0 ng g^{-1} in 15.3 g of 20vol% iAR. The sample was run in duplicate during two different days using dedicated UM-Almaden and ETH-Fluka standards, also at 8.0 ng g^{-1}. All individual sample and standard results are given in the Supplementary Data. The signals obtained on the ^{196}Hg and ^{202}Hg isotopes during these sessions were 15mV and 3 Volt. We recommend the use of 10^{12} or 10^{13} Ω resistors on the signal amplifier of the ^{196}Hg Faraday cup. The 2σ uncertainty, based on sample, UM-Almaden, and ETH-Fluka replicates, on Δ^{196}Hg during these analysis sessions were 0.19‰ (Table S3).

3. Results and discussion

3.1 GEM isotope compositions

The nine day sampling period from 19 to 28 Dec 2012 was characterized by a shift from cloudy conditions (days 1-2, samples D1-D5) to clear skies (days 3-5, samples D6-D10), and back to clouds (days 7-9, samples D11-D14). The wind direction was predominantly southwest bringing North-Atlantic Ocean air masses, over northwest Spain, to the PDM. The continuous Hg speciation observations show a pronounced increase in GOM

to 238 pg m^{-3} (60 h mean), and concurrent decrease in GEM during samples D6-D10 (clear skies, Figure 1, Table S1). Back trajectory analysis, and low observed relative humidity and CO, suggest that the high GOM concentrations represent the intrusion of a free tropospheric (FT) air mass that originated at 5000m (550hPa, Figures 1 and Figure S1). FT intrusions are typical at PDM, e.g. 61 similar events were registered over a one year period from Nov 2011 to Nov 2012.[29] The intrusions are of particular interest as they offer a snapshot of the free troposphere where GEM oxidation is thought to take place.[29, 39-41] δ^{202}Hg, Δ^{199}Hg and Δ^{200}Hg of 12h and 24h GEM samples collected from 19 to 28 Dec 2012 were in the range of 0.16 to 0.51‰ (δ^{202}Hg, mean = 0.34‰), -0.31 to -0.11‰ (Δ^{199}Hg, mean = -0.23‰), and -0.17 to 0.04‰ (Δ^{200}Hg, mean = -0.07‰) (Table S1). These observations are consistent with a single two-week integrated GEM isotope sample B19, collected over the same period 19 to 28 Dec 2012 at a lower flow rate of 2 L min^{-1} with δ^{202}Hg of 0.39‰, Δ^{199}Hg of -0.27‰, Δ^{200}Hg of -0.10 ‰.[42]

3.2 RM, cloud water and rainfall Hg isotope compositions

In a previous study we found that Pyrenees rainfall Hg isotope signatures 150km east from the PDM are typical of rainfall observations globally, with a mean δ^{202}Hg of 0.17 ± 0.35 ‰ and significant odd MIF (Δ^{199}Hg = 0.72 ± 0.15 ‰; Δ^{201}Hg = 0.76 ± 0.15 ‰) and even-MIF (Δ^{200}Hg = 0.21 ± 0.04 ‰; Δ^{204}Hg = -0.33 ± 0.10 ‰, all mean ± 1σ, n = 9) (Figure 2, Table S2).[27] Here we find that PDM cloud water THg concentrations and MDF and MIF signatures (Table S3) are not significantly different from PDM regional rainfall (t-test, *p* values = 0.26 to 0.79). For the first time we observe that RM, i.e. GOM+PBM, at PDM also has positive odd MIF (Δ^{199}Hg = 0.44 ± 0.17 ‰; Δ^{201}Hg = 0.44 ± 0.10 ‰) and even-MIF (Δ^{200}Hg = 0.15 ± 0.06 ‰; Δ^{204}Hg = -0.22 ± 0.17 ‰, all 1σ, n = 12, Table S3), similar to PDM cloud water and rainfall (Figure 2) and similar to global rainfall (Δ^{199}Hg = 0.35 ± 0.19 ‰; Δ^{200}Hg = 0.14 ± 0.06 ‰; Δ^{201}Hg = 0.35 ± 0.20 ‰ (18). The RM, cloud water and GEM data, together with previous PDM observations, define a Δ^{199}Hg/Δ^{201}Hg slope of ~ 1.0 (Figure 2d), thought to be diagnostic of aqueous inorganic photoreduction of Hg-DOC (dissolved organic carbon) compounds.[21, 43] In a recent study, based on equilibrium thermodynamic speciation calculations and Hg reduction kinetics, we suggested that Hg-DOC complexes are indeed the dominant species in atmospheric waters.[35] Demers et al. were the first to point out a negative correlation between Δ^{200}Hg and Δ^{204}Hg in rainfall, with a slope of approximately -0.5.[26] Our work at the PDM extends this relationship to RM and cloud water phases (Figure 2c, slope = -0.52). The presence of even- and odd-MIF in RM suggests that globally observed Hg MIF signatures in rainfall are likely inherited from RM. Equally important, the isotopic composition of RM is in stark contrast with that of

GEM (Figure 2), even though the only transformation that separates the two forms of Hg is net oxidation. This corroborates the suggestion that net photochemical oxidation of GEM is responsible for even-Hg MIF,[24] but it does not identify the oxidative or reductive nature of the MIF inducing step among the myriad of possible reactions that drive atmospheric net GEM oxidation.

Cloud water and rainfall δ^{202}Hg (0.14 ± 0.29 ‰) and Δ^{199}Hg (0.74 ± 0.19 ‰) show significant enrichment in the heavier and in the odd Hg isotopes relative to mean RM δ^{202}Hg (-0.73 ± 0.63 ‰) and Δ^{199}Hg (0.44 ± 0.18 ‰) (t-test, both δ^{202}Hg and Δ^{199}Hg $p < 0.001$, all mean ± 1σ, Tables S2 and S3). We investigated if this is caused by in-cloud Hg^{II} photoreduction, by incubating an urban rainfall sample from Toulouse spiked with 103 ng L^{-1} of NIST 3133 Hg. The spike was equilibrated for 24h in the dark. Then, after 24h exposure to artificial sunlight from a Xe lamp while continuously purging product Hg^0 with argon, the rainfall Hg concentration had dropped to 78 ng L^{-1} and small positive shifts in δ^{202}Hg (0.15 ‰), Δ^{199}Hg (0.10‰), and Δ^{201}Hg (0.11‰), but not Δ^{200}Hg (-0.03‰) were detected (Table S3). The pseudo-first order gross Hg photoreduction rate constant for the experiment was low, 0.03 h^{-1}, which is in the range (0.05 ± 0.02 h^{-1}, 1σ, n=9) of other urban rainfall photoreduction rates, but slower than surface water rates of 0.41 h^{-1}.[12, 35] Bergquist & Blum (2007) determined experimental aqueous Hg photoreduction rates at 1000x higher Hg concentrations and Hg to DOC ratios, and showed faster photoreduction rates of 0.47 h^{-1}, and MDF and odd-MIF fractionation factors, $\varepsilon^{202/198}_{MDF(GOM-GEM)}$ of -0.6 to -0.8‰, $\varepsilon^{199/198}_{MIF(GOM-GEM)}$ of -1.0‰, and $\varepsilon^{201/198}_{MIF(GOM-GEM)}$ of -0.5 to -1.0‰. Despite our slower reduction rate, explained by our lower Hg to DOC ratio (i.e. stronger Hg-DOC bonds), we observed similar fractionation factors of -0.6, -0.4 and -0.4‰ respectively. Other Hg^{II} photoreduction experiments with lake water produced MIF factors ranging from -1.6 to -6.6‰.[22] Even-Hg MIF was not significant in our photochemistry experiment, nor in published work on surface waters.[21, 22] Based on current evidence, we therefore exclude photochemical Hg^{II} reduction in cloud droplets as the origin for even-Hg MIF. More experimental work is needed to reproduce atmospheric aqueous odd-Hg MIF, and explore variability in odd-MIF factors.

Finally, we examined PDM data variability in Δ^{200}Hg vs Δ^{199}Hg space, which in early work on rainfall Hg and GEM indicated a potentially diagnostic Δ^{199}Hg/Δ^{200}Hg slope of approximately 1.9.[25] While we observe an overall similar Δ^{199}Hg/Δ^{200}Hg slope, of 3.3 (Figure 2e) across the oxidized and reduced Hg phases at PDM, the GEM data alone clearly show different behavior: the GEM Δ^{199}Hg/Δ^{200}Hg and Δ^{201}Hg/Δ^{200}Hg (not shown) slopes are 1.10 ± 0.17, and 0.92 ± 0.24 (2σ) respectively. This suggests that the atmospheric mechanism that caused even-Hg MIF was possibly accompanied by odd-Hg MIF of similar magnitude, yet smaller than the odd-

MIF that separates the Hg^0 and Hg^{II} pools. This implies that the opposite odd-Hg MIF displayed by the oxidized and reduced Hg pools on the whole (Figure 2e) was acquired during a different atmospheric Hg transformation than the reaction that caused even Hg-MIF. In the case that even-Hg MIF occurs in the stratosphere, the small imprint that it leaves on the stratospheric Hg^0 pool will slowly mix down into the tropospheric Hg^0 pool. The PDM Hg^0 data spread and $\Delta^{199}Hg/\Delta^{200}Hg$ slope of 1.10 (Figure 2e) may therefore partially represent a mixing line between recently emitted Hg^0 and older, stratospherically processed Hg^0.

3.3 Hg isotope variation during the free troposphere intrusion event

We further examined atmospheric odd and even Hg MIF variability in the high frequency (12-24h) GEM isotope observations during the free tropospheric air mass intrusion, enriched in GOM and depleted in GEM (Figure 1, samples D6-D10). The FT intrusion event showed GOM concentrations of 238 pg m^{-3} from 22-25 Dec (60h mean). The intrusion event was accompanied by low CO concentrations, depleted GEM concentrations, and low relative humidity (Figure 1 and Figure S1), which is consistent with previous studies and indicative of GOM production by oxidation of GEM in a free tropospheric air mass.[44, 45] Seven-day back-trajectories of the FT intrusion and of the pre- (samples D1-D5) and post-event (D11-D14) air masses illustrate the important control of altitude and cloudiness along the trajectory on detected GOM levels at the PDM (Figure S1). Pre/post-FT intrusion event air masses generally travelled at 700-1000 hPa (3000 m – 0 m asl) over the N-Atlantic Ocean (35-50° N) with RH from 60-100% and daytime solar radiation <200 W m^{-2} suggestive of GOM scavenging by clouds (Figure 1 and Figure S1). FT intrusion air masses also travelled over the subtropical N-Atlantic Ocean, though at lower latitudes (20-35° N), and higher altitudes of 500-900 hPa (5500 m – 1500 m asl) with RH from 0-40% and daytime solar radiation from 200-500 W m^{-2} suggestive of clear skies (Figure S1). FT intrusion mean ozone (47 ± 2 ppbv, sd), CO (83 ± 3 ppbv, sd) and relative humidity (34 ± 10%, sd) are typical of lower to middle free tropospheric air (Figure 1 and Table S1).

We examined the relationship between reactant GEM and product GOM concentration, in order to assess product GOM removal and the extent of net GEM oxidation. A negative correlation between GEM and GOM was observed during the 8-day study period of Dec 2012 with GOM/GEM slope of -0.44 ± 0.10 (r^2 = 0.66; Figure S2). It has been previously suggested that GOM/GEM slopes higher than -1 reflect the loss of newly produced GOM by scavenging processes, or the mixing with other air masses with different GEM levels.[39, 40] PBM concentrations during the FT intrusion event are uniformly low (mean: 4 pg m^{-3}) and RH and solar radiation levels along the back trajectories do not support an important scavenging sink (Figure S1 and Table

S1). A prerequisite for the GOM/GEM slope analysis is that the ensemble of observations has a common air mass origin, which is not the case here. The back trajectory analysis of our 8-day observations suggests partly overlapping altitudes for pre- and post-event (3000 m – 0 m asl) and FT-event (5500 m – 1500 m asl) air masses. Published reviews of GEM altitude profiles suggest little variation up to 5km.[9] However, observed and modeled boundary layer GEM levels suggest maximum levels between 30-60°N, corresponding to mid-latitude emission sources, and declining levels from 30° N to the equator (1% decrease in GEM per degree latitude).[9] As mentioned above pre/post-event and FT-event back trajectories point out different latitudinal origins of 20-35° N and 35-50° N respectively. It seems therefore plausible that the original GEM levels in pre/post-event and FT-event air masses were different due to different latitudinal air mass origins. A correction for latitudinal confounding allows estimating original GEM levels to be 15% lower in the FT-event air masses, based on the 1% drop in GEM per degree latitude, and yields a corrected GOM/GEM slope of -0.88 (Figure S2, gray line). The corrected slope is close to -1 and therefore suggests that nearly all GOM produced has been retained within the free tropospheric air masses observed during the FT-event at the PDM.

$\delta^{202}Hg_{GEM}$ and $\Delta^{204}Hg_{GEM}$ during the FT intrusion event are slightly but not significantly higher (t-test, $p > 0.05$), and $\Delta^{199}Hg_{GEM}$, $\Delta^{200}Hg_{GEM}$ and $\Delta^{201}Hg_{GEM}$ slightly but significantly lower (by 0.10, 0.06, 0.08‰ respectively, t-test, $p < 0.05$) than pre- and post-event samples during 20 - 28 Dec 2012 (Figure 1, Table S1). $\Delta^{199}Hg_{GEM}$, $\Delta^{200}Hg_{GEM}$ and $\Delta^{201}Hg_{GEM}$ are also significantly correlated with GEM and GOM concentration (r^2 of 0.6, 0.5, 0.4 and $p<0.05$). Because the FT-event was long-lived, displaying elevated GOM levels over 48 hours, we suggest that the GEM and GOM concentration, and GEM isotope observations represent a snapshot of net GEM oxidation that has been little influenced by further mixing with boundary layer air. Since the FT air masses originated from higher altitudes, the Hg MIF observations corroborate previous work on even-MIF in precipitation that suggested even-MIF to originate at the tropopause or stratosphere.[24] Although we cannot deconvolute and attribute even MIF and odd MIF to particular atmospheric reduction and oxidation reactions, we can estimate approximate net oxidation isotope enrichment factors for MDF and MIF that may be of use in atmospheric Hg isotope models. To do so, we combine our mean (± 1σ) GEM (FT intrusion) and RM isotope observations and calculate isotope enrichment factors by difference: $\varepsilon^{202/198}_{MDF(GOM-GEM)}$ of -1.1 ± 0.7‰, $\varepsilon^{199/198}_{MIF(GOM-GEM)}$ of 0.73 ± 0.23‰, $\varepsilon^{200/198}_{MIF(GOM-GEM)}$ of 0.26 ± 0.10‰, $\varepsilon^{201/198}_{MIF(GOM-GEM)}$ of 0.69 ± 0.14‰, and $\varepsilon^{204/198}_{MIF(GOM-GEM)}$ of -0.39 ± 0.22. We note that the RM isotopic composition was not collected simultaneously with the GEM isotope data, but that both RM and FT GEM represent our best estimates of the upper tropospheric

and lower stratospheric reduced and oxidized Hg pools.

3.4 Atmospheric Δ^{200}Hg mass balance

In global Hg box models and in 3D Hg cycling models the atmosphere is generally in steady-state, i.e. the mass of Hg in the atmosphere is constant and emission fluxes equal deposition fluxes.[3, 15, 46, 47] The reason for this is that the troposphere is a relatively small reservoir (4 Gg of Hg) compared to soils (1000 Gg) and oceans (300 Gg), exchange fluxes with continents and ocean are large (~8 Gg y^{-1}) and consequently the atmospheric lifetime is short (1y).[16] Hg emission and deposition budgets in models range from well-constrained (volcanic, anthropogenic emission, wet deposition over land) to ill-constrained (terrestrial, marine emissions and dry deposition over land and oceans). An estimate of natural and anthropogenic emission Δ^{200}Hg signatures suggests these were constant over the past 150 years.[48] Natural archives of atmospheric Hg deposition, such as sediment and peat cores, also suggest that atmospheric Δ^{200}Hg was generally constant during recent centuries.[49, 50] The steady-state in terms of Hg mass, i.e. emissions equal deposition, should therefore be accompanied by a steady-state in terms of Δ^{200}Hg where emission Δ^{200}Hg equals deposition Δ^{200}Hg. If this were not the case, atmospheric Δ^{200}Hg, and the Δ^{200}Hg of atmospheric Hg deposition would vary with time. In Table 1 we examine whether the steady-state Δ^{200}Hg condition is met for the state of the art Hg GEOS-Chem/MITgcm Hg cycling model.[3] Our new free tropospheric RM Δ^{200}Hg observations of 0.15 ± 0.06 ‰ allow to account for the large global RM dry deposition flux to land and oceans. We include additional non-urban aerosol and fog Δ^{200}Hg observations from previous studies to derive a global mean RM Δ^{200}Hg of 0.12 ± 0.05 ‰ (n = 66).[51-53] Marine and terrestrial Hg re-emissions are taken into account using published median Δ^{200}Hg of 0.05 and -0.01 ‰ for these pools respectively.[28, 54] We assume here that Δ^{200}Hg of Earth surface Hg^0 emissions equal the Δ^{200}Hg of the Earth surface pools, as the fractionation of Δ^{200}Hg takes place exclusively during upper atmospheric redox reactions. Total Hg emissions in the model are 8540 Mg/y and deposition 8500 Mg/y, confirming steady state. Using these global flux and Δ^{200}Hg data (Table 1), we calculate Hg emission Δ^{200}Hg to be 0.025 ± 0.032 ‰, and Hg deposition Δ^{200}Hg to be 0.073 ± 0.019 ‰ (1σ), which violates isotopic steady state. This likely suggests that model deposition Δ^{200}Hg is biased towards the RM dry and wet deposition end-members of 0.12 and 0.17 ‰. Recent terrestrial Δ^{200}Hg studies suggested that vegetation and soil Δ^{200}Hg is dominated by GEM deposition.[26, 27] We therefore propose that Hg cycling models need to better accommodate the Hg-isotope constraints on emission and deposition fluxes, in particular the more important role of GEM deposition compared to RM deposition.

3.5 Potential even Hg isotope MIF mechanisms

Even-Hg isotope MIF has become a useful tracer to constrain atmospheric Hg deposition pathways, reservoir size, or atmospheric conditions as illustrated above and elsewhere.[26-28, 49, 54, 55] The chemical reaction(s) and underlying even-MIF mechanism are however, far from understood. Two studies observed even-Hg MIF under relatively well-constrained conditions. Mead et al. observed even- and odd-MIF during Hg^0 oxidation in fluorescent lamps, attributing it partially to nuclear self-shielding, i.e. isotope fractionation as a function of isotope abundance.[56] Nuclear self-shielding considers that in a dense column of (Hg^0) gas, the photolysis yield of abundant isotopes is lower than the yield of low-abundance isotopes. Abundant $^{202}Hg^0$ absorbs UV-C radiation entirely, suppressing further $^{202}Hg^0$ photolysis to Hg^{II}. The oxidized Hg^{II} fraction, analyzed in the glass housing of the lamp, showed negative $\Delta^{199}Hg$, $\Delta^{200}Hg$, and positive $\Delta^{201}Hg$ and $\Delta^{204}Hg$, which contrasts with rainfall Hg^{II} MIF for 3 of the 4 signatures (Figure 3a).[56] We further investigated the self-shielding mechanism by analyzing for the first time the $\Delta^{196}Hg$ signature of a single, unique summertime thunderstorm rainfall sample that had both a high volume and relatively high THg concentration. We observe $\Delta^{196}Hg$ to be near-zero (-0.06 ± 0.19‰, 2σ, n = 2) in the 'GET rain 6' sample (Figure 3), which has pronounced $\Delta^{199}Hg$ (0.70‰), $\Delta^{200}Hg$ (0.25‰), $\Delta^{201}Hg$ (0.82‰), and $\Delta^{204}Hg$ (-0.45‰). The observation that the least abundant ^{196}Hg, and most abundant ^{202}Hg isotopes, both referenced to ^{198}Hg, show near-zero MIF, further suggests that nuclear self-shielding by trace atmospheric Hg^0 is unlikely to be the mechanism responsible for atmospheric Hg MIF.

In a remarkable experimental study, Sun et al. (2016) investigated Hg^0 oxidation by UV-B induced $Cl^\bullet$ and $Br^\bullet$ radicals, which are potentially important atmospheric Hg^0 oxidants, and observed even- and odd-Hg MIF in Hg^0 reactant and Hg^{II} products. The $\Delta^{199}Hg/\Delta^{201}Hg$ slope across Hg^0 and Hg^{II} data was 1.6 in the $Br^\bullet$ and 1.9 in the $Cl^\bullet$ experiment, and was suggested to predominantly reflect the nuclear volume effect (NVE). Both non-photochemical experimental studies and NVE numerical simulations indicate NVE $\Delta^{199}Hg/\Delta^{201}Hg$ slopes to be around 1.6.[20, 57] NVE theory also predicts small even-Hg MIF with a potentially diagnostic $\Delta^{199}Hg/\Delta^{200}Hg$ slope of 6.4 (Figure 3b, based on Wiederhold et al.[20]). The observed $\Delta^{199}Hg/\Delta^{200}Hg$ slope for Hg^{II} in the $Cl^\bullet$ and $Br^\bullet$, and Hg^0 in the $Cl^\bullet$ experiments is however negative, -8.3 (Figure 3b). In other words, while $\Delta^{200}Hg$ in the Hg^{II} product was found to be positive, similar to atmospheric Hg^{II}, $\Delta^{199}Hg$ and $\Delta^{201}Hg$ were strongly negative and opposite to atmospheric Hg^{II}. Sun et al., considered the combined $\Delta^{199}Hg$ and $\Delta^{200}Hg$ incompatible with a magnetic isotope effect (MIE), but did mention that particulate Hg^{II} formation on the reactor wall could have facilitated a MIE. In the following we further explore the data from Sun et al. and speculate on an alternative

MIE mechanism for even-MIF during atmospheric Hg^{II} photoreduction that involves spin coupling between ^{even}Hg isotope free electrons and nearby magnetic nuclei.

The Hg^0 photo-oxidation experiments by Sun et al. are complex because multiple oxidation and reduction reactions occurred simultaneously in the reaction chamber (Figure 4). Hg^0 reacts with $Br^{\bullet}$ (or $Cl^{\bullet}$) into the $Hg^{I}Br^{\bullet}$ radical, which either thermally or photolytically degrades back into Hg^0 reactant or combines with a 2nd $Br^{\bullet}$ (or $Cl^{\bullet}$) to form stable $BrHg^{II}Br_{(g)}$. Sun et al. observed loss of Hg^{II} species to the FEP Teflon reactor wall, which complicated Hg mass and Hg isotope balance in the experiments: this is illustrated for Hg^0 reactant and Hg^{II} product in the $Br^{\bullet}$ experiments, which both have positive $\Delta^{200}Hg$ (Figure 3b). In Figure 4 we therefore consider reversible binding of $BrHg^{II}Br$ and $Hg^{I}Br$ to the surface (indicated by =). Here we also consider gas phase and surface photoreduction of $Hg^{I}Br$ and $BrHg^{II}Br$ compounds, following recent theoretical work. As indicated by Sun et al. the large odd-MIF observed in both $Cl^{\bullet}$ and $Br^{\bullet}$ experiments likely reflects a dominant NVE during one of the oxidation steps. We therefore estimated the small $\Delta^{200}Hg_{NVE}$ associated with oxidation by using the theoretical $\Delta^{199}Hg/\Delta^{200}Hg$ NVE slope of 6.4: $\Delta^{200}Hg_{res} = \Delta^{200}Hg_{obs} - \Delta^{199}Hg_{obs}/6.4$ (Figure 3b). The residual, $\Delta^{200}Hg_{res}$, gradually increases with net Hg^0 photo-oxidation progress (Figure 3c). We suggest that the surface $Hg^{I}Br$= and $Hg^{II}Br_2$= species (Figure 4) concentrations increased over time, leading to a parallel increase in photolysis of the same species that expressed even-Hg MIF ($\Delta^{200}Hg_{res}$). To summarize, it appears that atmospheric even- and odd-Hg MIF may be caused by different mechanisms and reactions: large odd-MIF by the MIE during aqueous Hg^{II} photoreduction (Figure 2d), potential small odd-MIF by the NVE during Hg^0 oxidation (Figure 3b), and potential small even-MIF during heterogeneous (surface) $Hg^{I,II}$ photoreduction. The multiple MIF mechanisms help explain why PDM Hg^0 and Hg^{II} (RM) data define relatively flat $\Delta^{199}Hg/\Delta^{200}Hg$ slopes of 1.2 and 0.0 (Figures 2e, 3b) that suggests even-MIF to possibly be an isolated phenomenon, accompanied by small odd-MIF. Next, we speculate on how heterogeneous Hg photoreduction might generate a MIE in non-magnetic even Hg isotopes.

Large ^{odd}Hg isotope MIF during DOC mediated aquatic photoreduction of Hg is generally thought to occur via the MIE.[21, 58, 59] A MIE occurs when the nuclear magnetic moment of ^{odd}Hg isotopes induces spin conversion of photo-excited $^{odd}Hg^{\bullet}$ free electrons by hyperfine spin coupling (HFC) with the electron magnetic moment. Spin conversion by HFC controls the fate of $^{odd/even}Hg^{\bullet\bullet}L$ radical pairs (where L is the coordinating ligand), by controlling break-up into free radicals or recombination into the original Hg-L reactant. The radical pair must be long-lived, generally caged in by water molecules or surface mobility constraints, for HFC to affect recombination rates. The MIE is therefore considered to be unlikely during gas phase reactions. Even Hg

isotopes generally have no nuclear magnetic moment and ($^{even}Hg^{\bullet\bullet}O)_{triplet}$ radical pairs are therefore generally considered insensitive to the MIE. Experimental and theoretical studies of Hg MIF by the MIE have thus far only considered the HFC of ^{odd}Hg isotope nuclear spin with ^{odd}Hg isotope free electrons. Unpaired electrons in radical pairs are however spread out over a portion of the molecular fragments of the radical pair, and interact with several magnetic nuclei simultaneously over distances up to 5Å.[60] For example, in the magnetoreception mechanism of migrating birds, photoexcited unpaired electrons of cryptochrome proteins are thought to interact, via HFC, with the molecular magnetic field of multiple magnetic ^{14}N and ^{1}H nuclei.[60] We therefore recognize that in the case of Hg photochemistry, HFC can in principle also occur between the spin of nearby magnetic nuclei and the unpaired electrons of both ^{even}Hg and ^{odd}Hg isotope radicals. In addition, magnetic Hg and ligand isotopes may also induce HFC and spin conversion in ligand free electrons, within a radical pair.

In Earth surface waters the aqueous coordination of inorganic divalent Hg is dominated by O and reduced S ligands on mineral surfaces and organic matter. These ligands have in common that their odd isotopes are not very abundant: ^{17}O, 0.04%; ^{33}S, 0.75%. Consequently, the potential influence of magnetic neighbor isotopes on $Hg^{\bullet}$ and $L^{\bullet}$ radical spin conversion has not been considered or formally investigated. In the atmosphere, however, Hg coordination is dominated by halogens, and N, in addition to O and possibly oxidized S (i.e. stratospheric SO_4 aerosols). Of particular interest here are the magnetic ^{1}H, ^{14}N, ^{35}Cl, ^{37}Cl, ^{79}Br, ^{81}Br and ^{127}I isotopes, which are all isotopically abundant, and possess nuclear spin. We therefore suggest that Cl and Br isotopes in the Sun et al. experiments, and possibly ^{1}H and ^{14}N isotopes in aerosols can induce HFC with radical pair free electrons of ^{odd}Hg, ^{even}Hg, and ^{odd}L, thereby influencing radical pair recombination rates and Hg MIF. It is still unclear how this would affect the relative even/odd Hg isotope sorting into Hg^0 and $Hg^{I,II}$ phases. HFC is strongly dependent on the free electron orbital, and on diffusional and rotational motion of the radical pair and/or neighboring ions.[61, 62] In heavy elements, electron orbitals are significantly affected by nuclear volume, yet the absence of $\Delta^{196}Hg$ in rainfall we show in this study, suggests that nuclear volume controlled HFC is unlikely; i.e. we would expect rainfall $\Delta^{196}Hg$ to be highly positive in that case, at opposite ends of the negative $\Delta^{204}Hg$ in rainfall. The strong nuclear magnetic moments of Br and I have been suggested to induce strong radical pair spin relaxation, by so called spin orbit coupling (SOC), preventing expression of the MIE.[63] While this is not the case for ^{1}H, ^{14}N, and $^{35,37}Cl$, photoreduction experiments with aqueous $HgCl_2$, and Hg-N compounds have thus far not shown even Hg-MIF.[58, 63] Despite its strong nuclear magnetic field, ^{1}H in H_2O molecules that hydrate HgL radical pairs in aqueous photoreduction experiments thus far,[22, 58, 63] have not led to even-Hg MIF. Similarly, the abundant presence of Cl ions in seawater does not appear to produce detectable

even- and odd-Hg MIF during marine Hg^{II} photoreduction. Finally, BrHgBr and ClHgCl only photolyse under UV-C radiation and HgBr and HgCl under UV-C, UV-B and VIS radiation. Since the Sun et al. experiments were done under UV-B radiation we attributed in Figure 4 the even-Hg MIE step to $Hg^{I}Br$ photolysis on the reactor wall. Despite several counter arguments against an even-Hg MIE mechanism, it does appear that the Sun et al. net Hg^{0} oxidation reactions have led to even-Hg MIF during surface mediated Hg photoreduction involving halogens. Possibly the interaction of free electron spin with neighboring odd halogen isotope nuclear spin in caged $Hg^{\bullet\bullet}Br$ compounds has a mass-independence related to non-statistical behavior during HFC or SOC that we can as of yet not explain. We encourage the issue to be further explored experimentally and theoretically.

■ Supporting Information

Additional information of the sampling site, sampling and processing, ancillary parameters, and air mass backward trajectories are presented in Supporting Information (Text S1-S4 and Figure S1-S3). All Hg stable isotope data measured and discussed in this study is reported in the Supplementary Data (Table S1-S3).

■ Author Information

Corresponding Author: jeroen.sonke@get.omp.eu (J.E.S)

■ Acknowledgements

This work was supported by research grants ERC-2010-StG-20091028, ERC-2015-PoC-665482 from the European Research Council and the H2020 ERA-PLANET (689443) iGOSP programme to JES. We acknowledge technical support from the UMS 831 Pic du Midi Observatory team. This observatory is part of the P2OA (http://p2oa.aero.obs-mip.fr). P2OA facilities and staff are funded and supported by the University Paul Sabatier Toulouse 3, France, and CNRS (Centre National de la Recherche Scientifique). XY thanks the Chinese Scholarship Council for his PhD fellowship. We thank Trond Saue at CNRS and Laura Motta at the University of Michigan for stimulating discussion on the concepts of nuclear spin – electron spin interaction. Three anonymous reviewers are thanked for their constructive comments.

Table 1. Δ^{200}Hg signatures of global Hg reservoirs, total Hg emissions and deposition. Tropospheric Hg reservoir, emission, and deposition fluxes are from Horowitz *et al.*[3] Mean Δ^{200}Hg and 1σ are from the following published data compilations: reactive Hg (RM) wet deposition, GEM, ocean Hg from Jiskra *et al.*;[28] anthropogenic GEM, RM emissions, volcanic GEM emissions, soil/vegetation Hg from Sun *et al.*;[54] RM dry deposition from this study. The combined uncertainty on calculated atmospheric GEM and RM fractions was propagated from uncertainties on fluxes and Δ^{200}Hg.

Tropospheric Hg reservoir		
GEM	Mg	3500
RM	Mg	400
Emission Flux		
GEM ocean→air	Mg/y	4600
RM land→air	Mg/y	1420
GEM anthropogenic	Mg/y	1470
GEM natural	Mg/y	250
RM anthropogenic	Mg/y	800
Total	Mg/y	8540
Deposition Flux		
GEM air→ocean	Mg/y	1700
GEM air→land	Mg/y	1200
RM air→ocean	Mg/y	4600
RM air→land	Mg/y	1000
Total	Mg/y	8500
Δ^{200}Hg value		
GEM	‰	-0.06 ± 0.03
RM wet deposition	‰	0.17 ± 0.05
RM dry deposition	‰	0.12 ± 0.05
GEM, RM Anthropogenic	‰	0.00 ± 0.03
GEM natural	‰	0.00 ± 0.03
Hg soil	‰	-0.01 ± 0.04
Hg ocean	‰	0.05 ± 0.03
Sum emission	‰	0.025 ± 0.032
Sum deposition	‰	0.073 ± 0.019

Figure 1. Hg speciation and isotope variability during a free tropospheric air mass intrusion. From 20 to 28 Dec 2012, high frequency (12h, 24h) gaseous elemental Hg^0 (GEM) isotope signatures $\delta^{202}Hg$, $\Delta^{199}Hg$, $\Delta^{200}Hg$ (A), CO and O_3 concentrations (B), atmospheric GOM, PBM and GEM concentrations (C), and solar radiation and relative air humidity (D) showed a 48h long intrusion of a free tropospheric air mass, high in GOM, and low in GEM and humidity. Fitted curves in panel (A) are smoothed splines, and the free troposphere intrusion events is shaded in gray color.

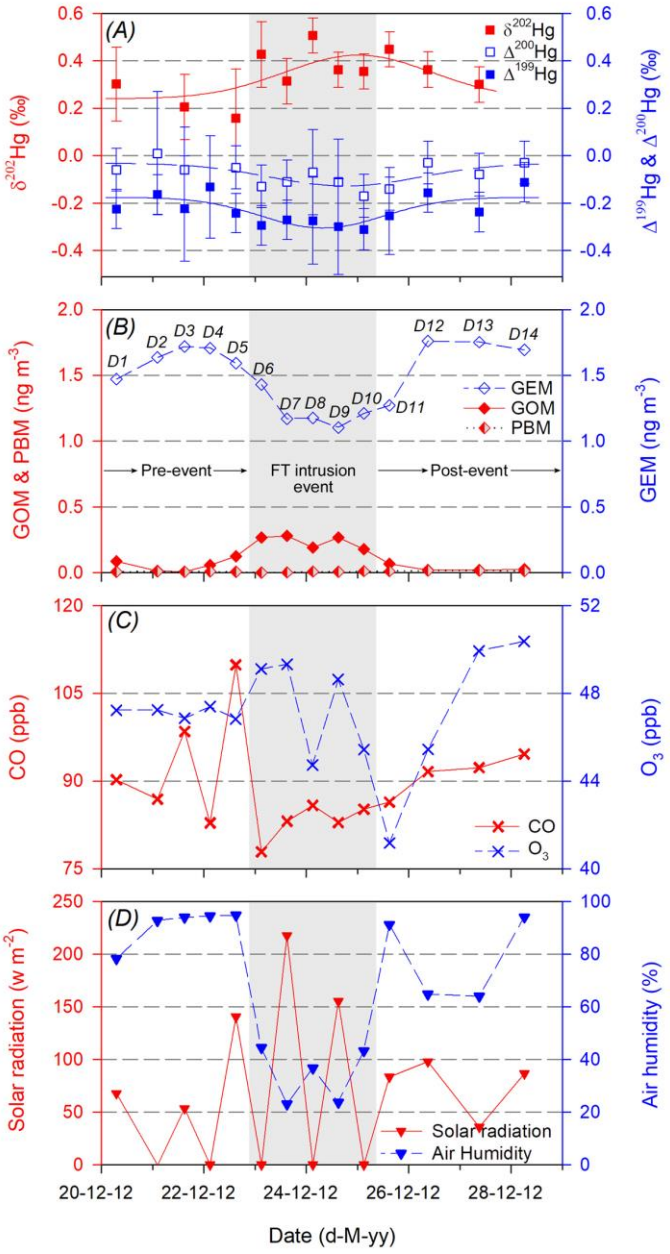

Figure 2. Atmospheric Hg stable isotope variation at the Pic du Midi. Hg mass dependent (δ^{202}Hg) and mass independent (Δ^{199}Hg, Δ^{200}Hg, Δ^{201}Hg, Δ^{204}Hg) isotope signatures in reactive Hg (RM=GOM+PBM), cloud water, 12h/24h GEM from this study, and previously published GEM and rainfall.[27, 42]

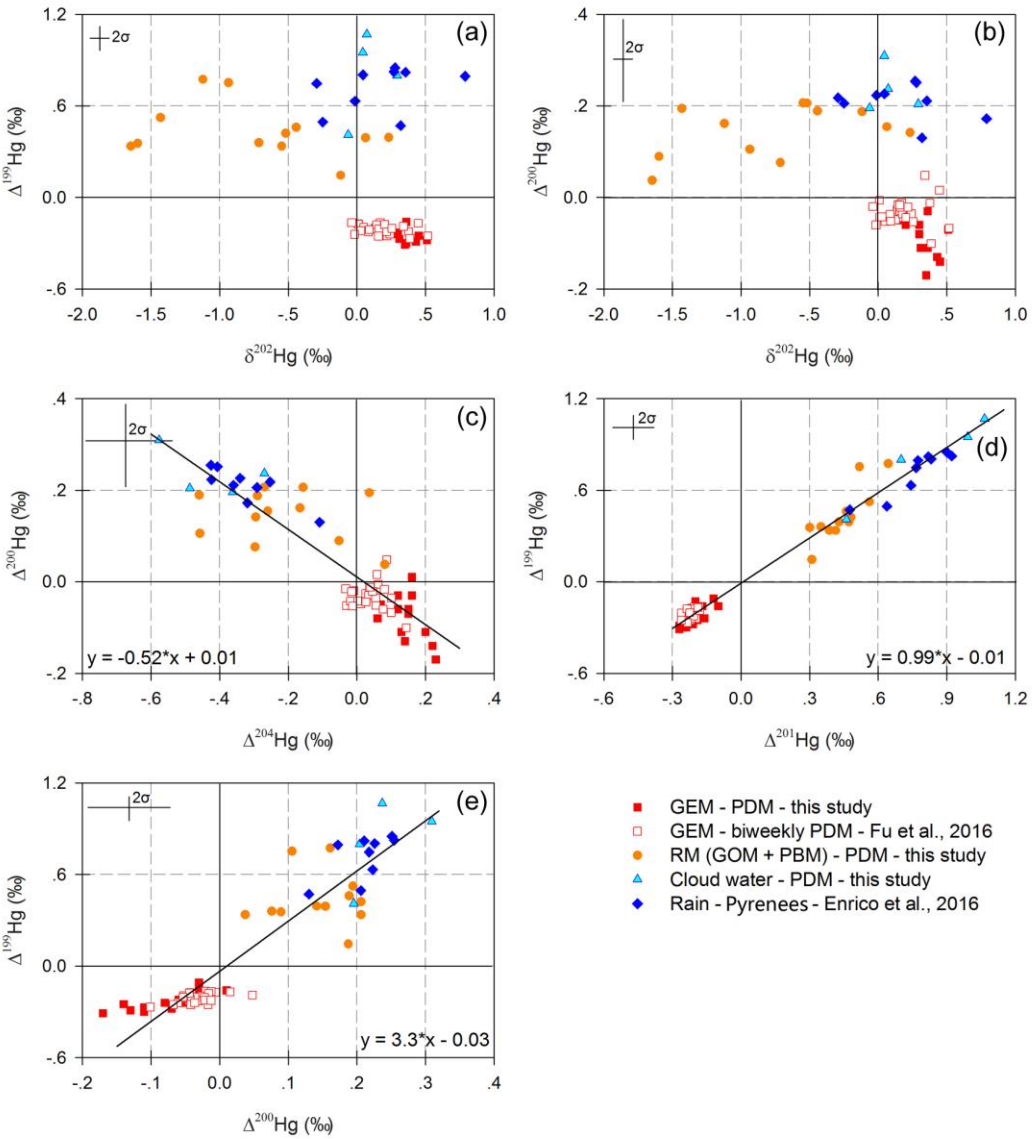

Figure 3. Hg MIF in rainfall vs. Hg oxidation MIF. a) Even- and off-Hg MIF in the 'GET rain 6' sample, in UV-oxidized Hg^{II} from a fluorescent lamp[56] (all $\Delta^{xxx}Hg$ divided by 20), and in $Cl^{\bullet}$ radical oxidized Hg^{II} .[64] The $\Delta^{xxx}Hg$ patterns of the two oxidation reactions are incompatible with rainfall observations, suggesting that nuclear self-shielding or nuclear volume fractionation are not the underlying cause of rainfall Hg^{II} MIF. $\Delta^{202}Hg$ equals 0 for all data in a) since the $\Delta^{xxx}Hg$ (where xxx are Hg isotopes masses 196 to 204) are calculated relative to $\delta^{202/198}Hg$ ratios, themselves anchored to the ^{198}Hg reference isotope. b) $\Delta^{199}Hg/\Delta^{200}Hg$ slopes of PDM Hg^0 data, theoretical NVE (6.4), and the $Cl^{\bullet}$ and $Br^{\bullet}$ oxidation experiments by Sun et al.[64] The parameter $\Delta^{200}Hg_{res}$ (‰) is defined as the residual $\Delta^{200}Hg$ after correcting the Sun et al. data for NVE c) $\Delta^{200}Hg_{res}$ variability as a function of net oxidation reaction progress in the Sun et al. data.[64]

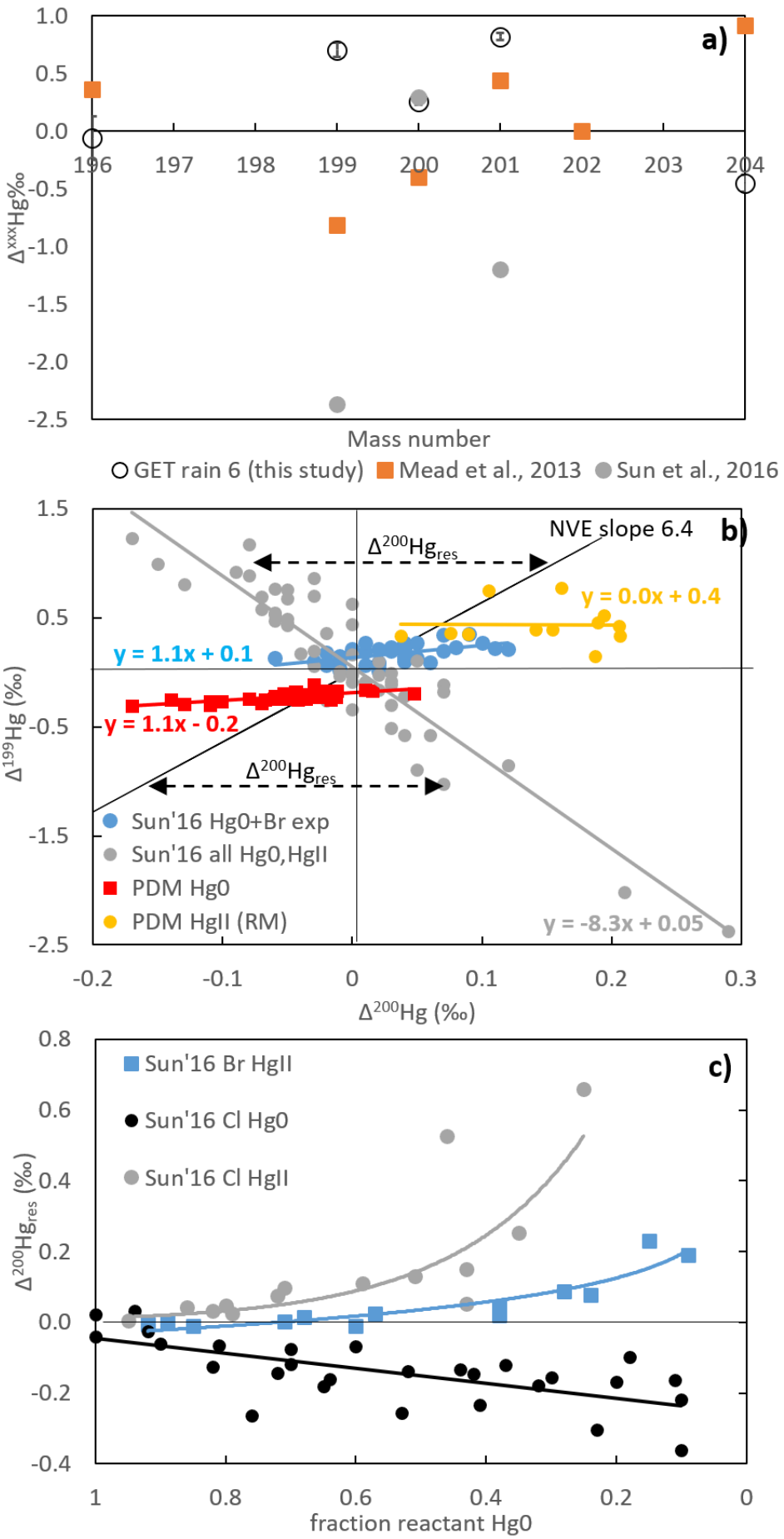
a)
1.0
0.5
0.0
-0.5
-1.0
-1.5
-2.0
-2.5
196
197
198
199
200
201
202
203
204
Δ^xxxHg‰
Mass number
GET rain 6 (this study)
Mead et al., 2013
Sun et al., 2016
b)
NVE slope 6.4
Δ200Hgres
y = 0.0x + 0.4
y = 1.1x + 0.1
y = 1.1x - 0.2
Δ200Hgres
Sun'16 Hg0+Br exp
Sun'16 all Hg0,HgII
PDM Hg0
PDM HgII (RM)
y = -8.3x + 0.05
1.5
0.5
-0.5
-1.5
-2.5
-0.2
-0.1
0
0.1
0.2
0.3
Δ199Hg (‰)
Δ200Hg (‰)
c)
Sun'16 Br HgII
Sun'16 Cl Hg0
Sun'16 Cl HgII
0.8
0.6
0.4
0.2
0.0
-0.2
-0.4
1
0.8
0.6
0.4
0.2
0
Δ200Hgres (‰)
fraction reactant Hg0

Figure 4. Scheme of potential oxidation (1, 3), thermal reduction (1), photo-reduction (*hv*, 2, 4, 7, 8) and reversible sorption (5, 6) reactions occurring during the 'net Hg0 photo-oxidation experiments by Sun et al (2016). 'M 'indicates bulk gas molecules, and '=' surface sorption sites. We speculate that even-Hg MIF, separating even ^{204}Hg and ^{200}Hg isotopes (step 9), occurs during surface bound Hg^{I}Br photolysis under the potential influence of ^{odd}Br nuclear spin HFC with ^{even}Hg free electron spin in a non-linear fashion with respect to atomic number. Photoreduction reaction rates 2, 4 and 7 are considered small relative to reaction 8. Superscripts 1 and 3 in Hg$^{\bullet\bullet}$Br radical pairs indicate singlet (↑↓) and triplet (↑↑) states of free electron spin.

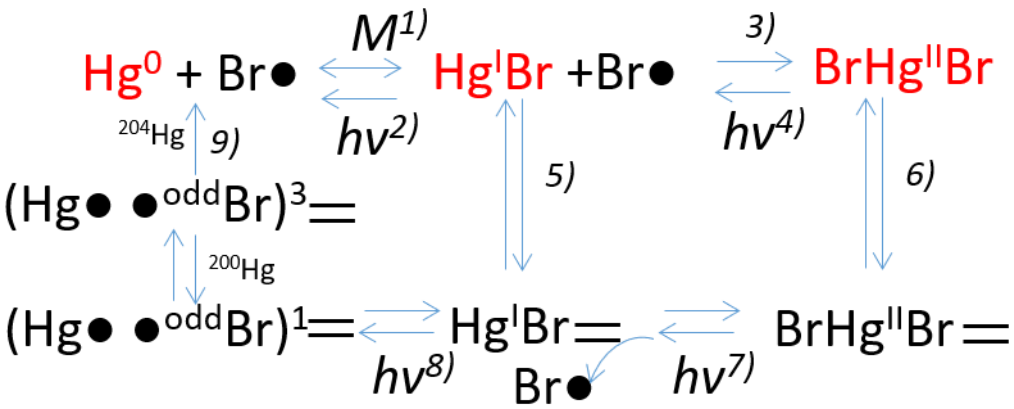

References

1. Streets, D. G.; Horowitz, H. M.; Lu, Z. F.; Levin, L.; ElsieMSunderland, C. P. T.; Sunderland, E. M., Five hundred years of anthropogenic mercury: spatial and temporal release profiles. *Environ Res Lett* **2019,** *14*, (8).
2. Li, C. X.; Sonke, J. E.; Le Roux, G.; Piotrowska, N.; Van der Putten, N.; Roberts, S. J.; Daley, T.; Rice, E.; Gehrels, R.; Enrico, M.; Mauquoy, D.; Roland, T. P.; De Vleeschouwer, F., Unequal Anthropogenic Enrichment of Mercury in Earth's Northern and Southern Hemispheres. *Acs Earth Space Chem* **2020,** *4*, (11), 2073-2081.
3. Horowitz, H. M.; Jacob, D. J.; Zhang, Y. X.; Dibble, T. S.; Slemr, F.; Amos, H. M.; Schmidt, J. A.; Corbitt, E. S.; Marais, E. A.; Sunderland, E. M., A new mechanism for atmospheric mercury redox chemistry: implications for the global mercury budget. *Atmos Chem Phys* **2017,** *17*, (10), 6353-6371.
4. Driscoll, C. T.; Mason, R. P.; Chan, H. M.; Jacob, D. J.; Pirrone, N., Mercury as a Global Pollutant: Sources, Pathways, and Effects. *Environmental Science & Technology* **2013,** *47*, (10), 4967-4983.
5. Munson, K. M.; Lamborg, C. H.; Boiteau, R. M.; Saito, M. A., Dynamic mercury methylation and demethylation in oligotrophic marine water. *Biogeosciences* **2018,** *15*, (21), 6451-6460.
6. Ariya, P. A.; Amyot, M.; Dastoor, A.; Deeds, D.; Feinberg, A.; Kos, G.; Poulain, A.; Ryjkov, A.; Semeniuk, K.; Subir, M.; Toyota, K., Mercury Physicochemical and Biogeochemical Transformation in the Atmosphere and at Atmospheric Interfaces: A Review and Future Directions. *Chem Rev* **2015,** *115*, (10), 3760-3802.
7. Dibble, T. S.; Tetu, H. L.; Jiao, Y. G.; Thackray, C. P.; Jacob, D. J., Modeling the OH-Initiated Oxidation of Mercury in the Global Atmosphere without Violating Physical Laws. *J Phys Chem A* **2020,** *124*, (2), 444-453.
8. Donohoue, D. L.; Bauer, D.; Cossairt, B.; Hynes, A. J., Temperature and pressure dependent rate coefficients for the reaction of Hg with Br and the reaction of Br with Br: A pulsed laser photolysis-pulsed laser induced fluorescence study. *J Phys Chem A* **2006,** *110*, (21), 6623-6632.
9. Holmes, C. D.; Jacob, D. J.; Corbitt, E. S.; Mao, J.; Yang, X.; Talbot, R.; Slemr, F., Global atmospheric model for mercury including oxidation by bromine atoms. *Atmos Chem Phys* **2010,** *10*, (24), 12037-12057.
10. Seigneur, C.; Vijayaraghavan, K.; Lohman, K.; Karamchandani, P.; Scott, C., Global source attribution for mercury deposition in the United States. *Environmental Science & Technology* **2004,** *38*, (2), 555-569.
11. Wang, F.; Saiz-Lopez, A.; Mahajan, A. S.; Martin, J. C. G.; Armstrong, D.; Lemes, M.; Hay, T.; Prados-Roman, C., Enhanced production of oxidised mercury over the tropical Pacific Ocean: a key missing oxidation pathway. *Atmos Chem Phys* **2014,** *14*, (3), 1323-1335.
12. Saiz-Lopez, A.; Sitkiewicz, S. P.; Roca-Sanjuan, D.; Oliva-Enrich, J. M.; Davalos, J. Z.; Notario, R.; Jiskra, M.; Xu, Y.; Wang, F.; Thackray, C. P.; Sunderland, E. M.; Jacob, D. J.; Travnikov, O.; Cuevas, C. A.; Acuna, A. U.; Rivero, D.; Plane, J. M. C.; Kinnison, D. E.; Sonke, J. E., Photoreduction of gaseous oxidized mercury changes global atmospheric mercury speciation, transport and deposition. *Nat Commun* **2018,** *9*.
13. Jaffe, D. A.; Lyman, S.; Amos, H. M.; Gustin, M. S.; Huang, J. Y.; Selin, N. E.; Levin, L.; ter Schure, A.; Mason, R. P.; Talbot, R.; Rutter, A.; Finley, B.; Jaegle, L.; Shah, V.; McClure, C.; Arnbrose, J.; Gratz, L.; Lindberg, S.; Weiss-Penzias, P.; Sheu, G. R.; Feddersen, D.; Horvat, M.; Dastoor, A.; Hynes, A. J.; Mao, H. T.; Sonke, J. E.; Slemr, F.; Fisher, J. A.; Ebinghaus, R.; Zhang, Y. X.; Edwards, G., Progress on Understanding Atmospheric Mercury Hampered by Uncertain Measurements. *Environmental Science & Technology* **2014,** *48*, (13), 7204-7206.
14. Weiss-Penzias, P.; Amos, H. M.; Selin, N. E.; Gustin, M. S.; Jaffe, D. A.; Obrist, D.; Sheu, G. R.; Giang, A., Use of a global model to understand speciated atmospheric mercury observations at five high-elevation sites (vol 15, pg 1161, 2015). *Atmos Chem Phys* **2015,** *15*, (4), 2225-2225.
15. Zhang, Y. X.; Horowitz, H.; Wang, J. C.; Xie, Z. Q.; Kuss, J.; Soerensen, A. L., A Coupled Global Atmosphere-Ocean Model for Air-Sea Exchange of Mercury: Insights into Wet Deposition and Atmospheric Redox Chemistry. *Environmental Science & Technology* **2019,** *53*, (9), 5052-5061.
16. Outridge, P. M.; Mason, R. P.; Wang, F.; Guerrero, S.; Heimburger-Boavida, L. E., Updated Global and Oceanic

Mercury Budgets for the United Nations Global Mercury Assessment 2018. *Environmental Science & Technology* **2018,** *52*, (20), 11466-11477.

17. Kwon, S. Y.; Blum, J. D.; Yin, R.; Tsui, M. T. K.; Yang, Y. H.; Choi, J. W., Mercury stable isotopes for monitoring the effectiveness of the Minamata Convention on Mercury. *Earth-Science Reviews* **2020,** *203*.

18. Jiskra, M.; Wiederhold, J. G.; Skyllberg, U.; Kronberg, R. M.; Hajdas, I.; Kretzschmar, R., Mercury Deposition and Re-emission Pathways in Boreal Forest Soils Investigated with Hg Isotope Signatures. *Environmental Science & Technology* **2015,** *49*, (12), 7188-7196.

19. Kritee, K.; Blum, J. D.; Reinfelder, J. R.; Barkay, T., Microbial stable isotope fractionation of mercury: A synthesis of present understanding and future directions. *Chem Geol* **2013,** *336*, 13-25.

20. Wiederhold, J. G.; Cramer, C. J.; Daniel, K.; Infante, I.; Bourdon, B.; Kretzschmar, R., Equilibrium Mercury Isotope Fractionation between Dissolved Hg(II) Species and Thiol-Bound Hg. *Environmental Science & Technology* **2010,** *44*, (11), 4191-4197.

21. Bergquist, B. A.; Blum, J. D., Mass-dependent and -independent fractionation of Hg isotopes by photoreduction in aquatic systems. *Science* **2007,** *318*, (5849), 417-420.

22. Zheng, W.; Hintelmann, H., Mercury isotope fractionation during photoreduction in natural water is controlled by its Hg/DOC ratio. *Geochim Cosmochim Ac* **2009,** *73*, (22), 6704-6715.

23. Zheng, W.; Hintelmann, H., Nuclear Field Shift Effect in Isotope Fractionation of Mercury during Abiotic Reduction in the Absence of Light. *J Phys Chem A* **2010,** *114*, (12), 4238-4245.

24. Chen, J. B.; Hintelmann, H.; Feng, X. B.; Dimock, B., Unusual fractionation of both odd and even mercury isotopes in precipitation from Peterborough, ON, Canada. *Geochim Cosmochim Ac* **2012,** *90*, 33-46.

25. Gratz, L. E.; Keeler, G. J.; Blum, J. D.; Sherman, L. S., Isotopic composition and fractionation of mercury in Great Lakes precipitation and ambient air. *Environmental Science & Technology* **2010,** *44*, (20), 7764-7770.

26. Demers, J. D.; Blum, J. D.; Zak, D. R., Mercury isotopes in a forested ecosystem: Implications for air-surface exchange dynamics and the global mercury cycle. *Global Biogeochem Cy* **2013,** *27*, (1), 222-238.

27. Enrico, M.; Le Roux, G.; Marusczak, N.; Heimburger, L. E.; Claustres, A.; Fu, X. W.; Sun, R. Y.; Sonke, J. E., Atmospheric Mercury Transfer to Peat Bogs Dominated by Gaseous Elemental Mercury Dry Deposition. *Environmental Science & Technology* **2016,** *50*, (5), 2405-2412.

28. Jiskra, M.; Heimbürger-Boavida, L. E.; Desgranges, M. M.; Petrova, M. V.; Dufour, A.; Araujo, B. F.; Masbou, J.; Chmeleff, E.; Thyssen, M.; Point, D.; Sonke, J. E., Mercury stable isotope composition of seawater suggests important net gaseous elemental mercury uptake. *EarthArXiv* **2020**.

29. Fu, X. W.; Marusczak, N.; Heimburger, L. E.; Sauvage, B.; Gheusi, F.; Prestbo, E. M.; Sonke, J. E., Atmospheric mercury speciation dynamics at the high-altitude Pic du Midi Observatory, southern France. *Atmos. Chem. Phys.* **2016,** *16*, (9), 5623-5639.

30. Fu, X. W.; Heimburger, L. E.; Sonke, J. E., Collection of atmospheric gaseous mercury for stable isotope analysis using iodine- and chlorine-impregnated activated carbon traps. *J Anal Atom Spectrom* **2014,** *29*, (5), 841-852.

31. Marusczak, N.; Sonke, J. E.; Fu, X. W.; Jiskra, M., Tropospheric GOM at the Pic du Midi Observatory-Correcting Bias in Denuder Based Observations. *Environmental Science & Technology* **2017,** *51*, (2), 863-869.

32. Sun, R. Y.; Enrico, M.; Heimburger, L. E.; Scott, C.; Sonke, J. E., A double-stage tube furnace-acid-trapping protocol for the pre-concentration of mercury from solid samples for isotopic analysis. *Anal Bioanal Chem* **2013,** *405*, (21), 6771-6781.

33. Demoz, B. B.; Collett, J. L.; Daube, B. C., On the Caltech Active Strand Cloudwater Collectors. *Atmos Res* **1996,** *41*, (1), 47-62.

34. Obrist, D.; Agnan, Y.; Jiskra, M.; Olson, C. L.; Colegrove, D. P.; Hueber, J.; Moore, C. W.; Sonke, J. E.; Helmig, D., Tundra uptake of atmospheric elemental mercury drives Arctic mercury pollution. *Nature* **2017,** *547*, (7662), 201-204.

35. Yang, X.; Jiskra, M.; Sonke, J. E., Experimental rainwater divalent mercury speciation and photoreduction rates in the presence of halides and organic carbon. *Sci Total Environ* **2019,** *697*.

36. Jiskra, M.; Sonke, J. E.; Agnan, Y.; Helmig, D.; Obrist, D., Insights from mercury stable isotopes on terrestrial-atmosphere exchange of Hg(0) in the Arctic tundra. *Biogeosciences* **2019,** *16*, (20), 4051-4064.

37. Blum, J. D.; Bergquist, B. A., Reporting of variations in the natural isotopic composition of mercury. *Anal Bioanal Chem* **2007,** *388*, (2), 353-359.

38. Blum, J. D.; Johnson, M. W., Recent Developments in Mercury Stable Isotope Analysis. *Reviews in Mineralogy & Geochemistry* **2017,** *82*, 733-757.

39. Lyman, S. N.; Jaffe, D. A., Formation and fate of oxidized mercury in the upper troposphere and lower stratosphere. *Nat Geosci* **2012,** *5*, (2), 114-117.

40. Swartzendruber, P. C.; Jaffe, D. A.; Prestbo, E. M.; Weiss-Penzias, P.; Selin, N. E.; Park, R.; Jacob, D. J.; Strode, S.; Jaegle, L., Observations of reactive gaseous mercury in the free troposphere at the Mount Bachelor Observatory. *J Geophys Res-Atmos* **2006,** *111, D24301*.

41. Timonen, H.; Ambrose, J. L.; Jaffe, D. A., Oxidation of elemental Hg in anthropogenic and marine airmasses. *Atmos. Chem. Phys.* **2013,** *13*, (5), 2827-2836.

42. Fu, X. W.; Marusczak, N.; Wang, X.; Gheusi, F.; Sonke, J. E., Isotopic Composition of Gaseous Elemental Mercury in the Free Troposphere of the Pic du Midi Observatory, France. *Environmental Science & Technology* **2016,** *50*, (11), 5641-5650.

43. Sonke, J. E., A global model of mass independent mercury stable isotope fractionation. *Geochim Cosmochim Ac* **2011,** *75*, (16), 4577-4590.

44. Gratz, L. E.; Ambrose, J. L.; Jaffe, D. A.; Shah, V.; Jaegle, L.; Stutz, J.; Festa, J.; Spolaor, M.; Tsai, C.; Selin, N. E.; Song, S.; Zhou, X.; Weinheimer, A. J.; Knapp, D. J.; Montzka, D. D.; Flocke, F. M.; Campos, T. L.; Apel, E.; Hornbrook, R.; Blake, N. J.; Hall, S.; Tyndall, G. S.; Reeves, M.; Stechman, D.; Stell, M., Oxidation of mercury by bromine in the subtropical Pacific free troposphere. *Geophys Res Lett* **2015,** *42*, (23).

45. Shah, V.; Jaegle, L.; Gratz, L. E.; Ambrose, J. L.; Jaffe, D. A.; Selin, N. E.; Song, S.; Campos, T. L.; Flocke, F. M.; Reeves, M.; Stechman, D.; Stell, M.; Festa, J.; Stutz, J.; Weinheimer, A. J.; Knapp, D. J.; Montzka, D. D.; Tyndall, G. S.; Apel, E. C.; Hornbrook, R. S.; Hills, A. J.; Riemer, D. D.; Blake, N. J.; Cantrell, C. A.; Mauldin, R. L., Origin of oxidized mercury in the summertime free troposphere over the southeastern US. *Atmos Chem Phys* **2016,** *16*, (3), 1511-1530.

46. Amos, H. M.; Jacob, D. J.; Streets, D. G.; Sunderland, E. M., Legacy impacts of all-time anthropogenic emissions on the global mercury cycle. *Global Biogeochem Cy* **2013,** *27*, (2), 410-421.

47. Semeniuk, K.; Dastoor, A., Development of a global ocean mercury model with a methylation cycle: Outstanding issues. *Global Biogeochem Cy* **2017,** *31*, (2), 400-433.

48. Sun, R. Y.; Streets, D. G.; Horowitz, H. M.; Amos, H. M.; Liu, G. J.; Perrot, V.; Toutain, J. P.; Hintelmann, H.; Sunderland, E. M.; Sonke, J. E., Historical (1850–2010) mercury stable isotope inventory from anthropogenic sources to the atmosphere. *Elem. Sci. Anth* **2016,** *4*, (91), 1-15.

49. Enrico, M.; Le Roux, G.; Heimburger, L. E.; Van Beek, P.; Souhaut, M.; Chmeleff, J.; Sonke, J. E., Holocene Atmospheric Mercury Levels Reconstructed from Peat Bog Mercury Stable Isotopes. *Environmental Science & Technology* **2017,** *51*, (11), 5899-5906.

50. Kurz, A. Y.; Blum, J. D.; Washburn, S. J.; Baskaran, M., Changes in the mercury isotopic composition of sediments from a remote alpine lake in Wyoming, USA. *Sci Total Environ* **2019,** *669*, 973-982.

51. Washburn, S. J.; Blum, J. D.; Motta, L. C.; Bergquist, B. A.; Weiss-Penzias, P., Isotopic Composition of Hg in Fogwaters of Coastal California. *Environmental Science & Technology Letters* **2021,** *8*, (1), 3-8.

52. Yu, B.; Yang, L.; Wang, L. L.; Liu, H. W.; Xiao, C. L.; Liang, Y.; Liu, Q.; Yin, Y. G.; Hu, L. G.; Shi, J. B.; Jiang, G. B., New evidence for atmospheric mercury transformations in the marine boundary layer from stable mercury isotopes.

Atmos Chem Phys **2020,** *20*, (16), 9713-9723.

53. Rolison, J. M.; Landing, W. M.; Luke, W.; Cohen, M.; Salters, V. J. M., Isotopic composition of species-specific atmospheric Hg in a coastal environment. *Chem Geol* **2013,** *336*, 37-49.

54. Sun, R. Y.; Jiskra, M.; Amos, H. M.; Zhang, Y. X.; Sunderland, E. M.; Sonke, J. E., Modelling the mercury stable isotope distribution of Earth surface reservoirs: Implications for global Hg cycling. *Geochim Cosmochim Ac* **2019,** *246*, 156-173.

55. Zerkle, A. L.; Yin, R. S.; Chen, C. Y.; Li, X. D.; Izon, G. J.; Grasby, S. E., Anomalous fractionation of mercury isotopes in the Late Archean atmosphere. *Nat Commun* **2020,** *11*, (1).

56. Mead, C.; Lyons, J. R.; Johnson, T. M.; Anbar, A. D., Unique Hg Stable Isotope Signatures of Compact Fluorescent Lamp-Sourced Hg. *Environmental Science & Technology* **2013,** *47*, (6), 2542-2547.

57. Ghosh, S.; Schauble, E. A.; Couloume, G. L.; Blum, J. D.; Bergquist, B. A., Estimation of nuclear volume dependent fractionation of mercury isotopes in equilibrium liquid-vapor evaporation experiments. *Chem Geol* **2013,** *336*, 5-12.

58. Zheng, W.; Hintelmann, H., Isotope fractionation of mercury during its photochemical reduction by low-molecular-weight organic compounds. *J Phys Chem A* **2010,** *114*, (12), 4246-53.

59. Buchachenko, A. L.; Ivanov, V. L.; Roznyatovskii, V. A.; Artamkina, G. A.; Vorob'ev, A. K.; Ustynyuk, Y. A., Magnetic isotope effect for mercury nuclei in photolysis of bis(p-trifluoromethylbenzyl)mercury. *Dokl Phys Chem* **2007,** *413*, 39-41.

60. Hore, P. J.; Mouritsen, H., The Radical-Pair Mechanism of Magnetoreception. *Annu Rev Biophys* **2016,** *45*, 299-344.

61. Grissom, C. B., Magnetic-Field Effects in Biology - a Survey of Possible Mechanisms with Emphasis on Radical-Pair Recombination. *Chem Rev* **1995,** *95*, (1), 3-24.

62. Turro, N. J., Influence of Nuclear-Spin on Chemical-Reactions - Magnetic Isotope and Magnetic-Field Effects (a Review). *Proceedings of the National Academy of Sciences of the United States of America-Physical Sciences* **1983,** *80*, (2), 609-621.

63. Motta, L. C.; Kritee, K.; Blum, J. D.; Tsz-Ki Tsui, M.; Reinfelder, J. R., Mercury Isotope Fractionation during the Photochemical Reduction of Hg(II) Coordinated with Organic Ligands. *The Journal of Physical Chemistry A* **2020,** *124*, (14), 2842-2853.

64. Sun, G.; Sommar, J.; Feng, X.; Lin, C.-J.; Ge, M.; Wang, W.; Yin, R.; Fu, X.; Shang, L., Mass-dependent and -independent fractionation of mercury isotope during gas-phase oxidation of elemental mercury vapor by atomic Cl and Br. *Environmental Science & Technology* **2016,** *50*, (17), 9232-9241.